# Nonlinear wave resonance due to oscillations of twin cylinders in a uniform current

H.C. Huang[1, 3], Y.F. Yang[2], R.H Zhu[1, 4], C.Z. Wang[1, 4, *]

[1] *Ocean College, Zhejiang University, Zhoushan, 316021, China*
[2] *Department of Mechanical Engineering, University College London, Torrington Place, London WC1E 7JE, UK*
[3] *Laboratory for Marine Geology, Qingdao National Laboratory for Marine Science and Technology, Qingdao 266061, China*
[4] *Yangjiang Offshore Wind Power Laboratory, Yangjiang, 529500, China*

## Abstract

A higher order finite element method with 8-node element is adopted to analyse the nonlinear wave resonance generated by oscillations of twin cylinders in a uniform current. The velocity potential in the fluid domain at each time step is obtained based on the finite element method through an iteration procedure. Numerical results are provided for twin rectangular cylinders undergoing specified oscillations in a uniform current at resonant frequencies. The effects of current on the wave and hydrodynamic force at the resonant frequencies are studied in detail and it is found that the resonance happens at all first-order resonant frequencies for both symmetric and antisymmetric motions of the cylinders. In particular, in addition to the first-order resonant frequency, the maximum wave elevation and horizontal force at resonance always regularly increase or decrease as the increase of the absolute value of Froude number or the spacing between two cylinders within the range of larger spacings. A similar trend can be also observed in the oscillational frequency of cylinders at resonance. Some results are also compared with those by linear solution and its superposition with the second-order, their difference at different Froude numbers are also discussed.

*Corresponding author, E-mail: cz_wang@zju.edu.cn (C.Z. Wang)

# 1. INTRODUCTION

Wave resonance is an interesting phenomenon in the field of hydrodynamics and it has important application in ocean engineering. The resonance happens when the wave frequency is equal to or even near the natural frequency of an ocean structure such as oil platforms. Correspondingly, large wave elevation and hydrodynamic forces are expected at resonance. A traditional approach to study wave resonance is through the perturbation method and quite a lot of works can be found in literature. For examples, Second-order resonances of sloshing waves in two-dimensional (2-D) and three dimensional (3-D) containers were analytically studied by Wu [1] and Zhang et al. [2], respectively. The linear and second-order resonances at nearly trapped modes were investigated by Maniar and Newman [3], Evans and Porter [4], Chen and Lee [5], Malenica et al. [6], Wang and Wu [7] and Kagemoto et al. [8]. Furthermore, recent attempts on two structures of side-by-side configuration can be found in Sun et al. [9], Watai et al. [10] and Zhao et al. [11].

Another approach to analyse wave-structure interaction is through the velocity potential theory with fully nonlinear boundary conditions. Wang and Wu [12] did research on wave resonance induced by two 2-D cylinders through the finite element method and it was found that wave elevations and hydrodynamic forces trend to be infinity when the perturbation method is applied, which is not in line with the actual situation. Inspired by this, the similar problem was further considered by Wang et al. [13] through the fully nonlinear numerical model. They found that both the wave elevation and hydrodynamic forces on the structures are much smaller than those obtained through the second-order theory. The amplitude of wave and force finally reach a constant value rather than become infinity when the time is sufficiently long. Later, Wang et al. [14] extended the work to the situation of multiple 2-D cylinders in vertical motions, while Li and Zhang [15] employed the boundary element method to study a similar problem that wave resonance generated by two 2-D barges in vertical motions. In addition to 2-D structures, typical study on wave resonance generated by 3-D floating bodies can be found in Sen [16] by a mixed Eulerian–Lagrangian panel method. The works mentioned above are all about wave resonance induced by the motion of floating structures. Besides, the resonance phenomena can be also observed in the problem of wave diffraction. For example, Bai et al. [17] simulated multiple cylinders diffracted by waves at nearly trapped frequencies. Ning et al. [18] and Feng and Bai [19] considered diffracted wave resonated by 2-D and 3-D multiple bodies in narrow gap respectively. In real engineering, the effects of viscosity may also be important to the wave resonance phenomenon. The main shortcoming of the viscous model is that it requires many computer resources. Wang et al. [20] studied wave resonance between two elongated parallel boxes with a narrow gap through experiment and viscous flow theory. Zhao et al. [21] also did experimental work on wave resonance within a narrow gap. Lu and Chen [22] added a dissipation coefficient to free surface boundary condition based on the potential theory and good results were achieved when compared with the experimental data. However, how to choose the dissipation coefficient depends on the experiment result and the numerical solution based on the viscous flow theory. Other typical works with considering vicious effects can be found in Lu et al. [23], Chua et al. [24] and Jiang et al. [25].

The aforementioned studies don't involve the current effect. It is well known that the wave frequency and amplitude will be affected by the presence of current. The effect is more obvious when the current speed is larger. Correspondingly, the waves and loads on ocean structures will be some or even significantly different from those without current, which will have important influence on the design of the ocean structures. Extensive works on wave-current-body interactions may be found in [26-31]. However, to the best of our knowledge, very little work is done for wave resonance with considering current effect. Fredriksen et al. [32] studied piston type resonance in a moonpool of two rectangular cylinders in vertical motions with a small gap at a low forward speed. In their work, both the experimental tests and numerical simulations are made to investigate resonant behaviour. Recently, Huang and Wang [33] studied two rectangular cylinders undergoing vertical and horizontal motions at resonant frequencies based on the second-order theory in the time domain. They found that the maximum wave elevation and hydrodynamic force generally decrease as the increases of Froude number and the nonlinearities become weaker. In addition, the resonant frequencies in both vertical and horizontal motions generally and slowly increase as the spacing between cylinders increases. Yang and Wang [34] also investigated the second-order wave diffraction by four vertical cylinders at near-trapping frequencies and found that the current effect on the wave and force is very clear, especially for the second-order components.

In this paper, we consider the problem of wave resonance by vertical and horizontal motions of two rectangular cylinders in a steady current. Compared with the investigation through the perturbation procedure in Huang and Wang [33], a fully nonlinear potential flow model is employed and more detailed analyses in physics are made for the current effect. Although the fully nonlinear potential theory usually overpredicts results about wave and hydrodynamic force when compared with the experiment data or the simulation based on the viscous flow theory. However, it can still provide meaningful results in describing the behaviour of wave and hydrodynamic force to show the relation between the wave or force peak and the current speed, the oscillational frequency, the oscillational amplitude and the gap between structures. The influence of current on the magnitude of the oscillational frequency at resonance, as well as on the value and nonlinearities of wave & hydrodynamic force are further discussed. Besides, a comparison is made for the similarities and differences between parts of the present nonlinear results and the second-order solutions. The present study may provide useful results about wave-current loads on multi-hulled ships and two approaching offshore structures in wave-current environment.

The paper is organized as follows. The mathematical model of the problem is presented in Section 2. The finite element method applied to discretize the governing equation is introduced in Section. 3. The numerical results are given in Section 4. In particular, the wave resonances induced by vertical oscillations are discussed in Section 4.1, while those by horizontal oscillations are analysed in Section 4.2.

## 2. MATHMATICAL FORMULATION

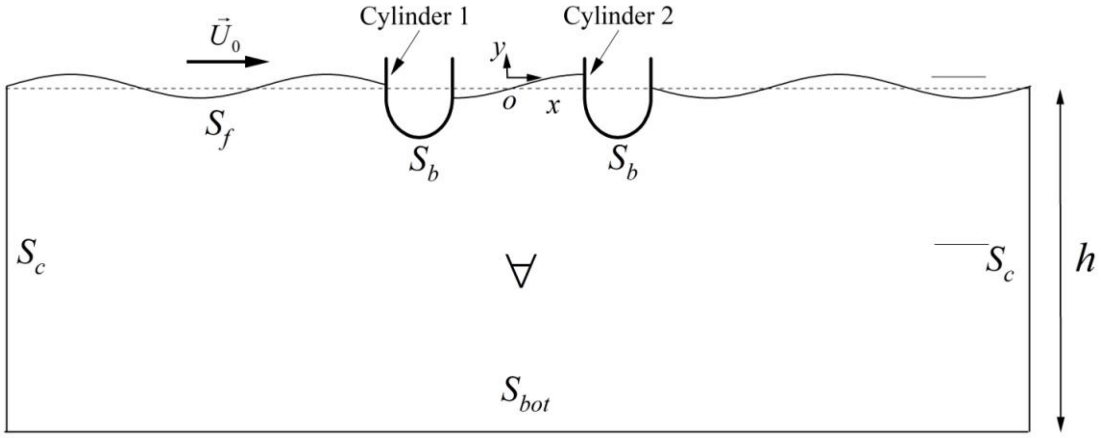


**Fig. 1.** Coordinate system.

Wave radiation by twin cylinders in forced motions is considered here. A right-handed Cartesian coordinate system *o*-*xy* is defined in Fig. 1, in which *x* is on the still water level and *y* points upward and is perpendicular to the *x*-axis. The surface of each cylinder is denoted as $S_b$, on which the unit normal vector of any point is $\vec{n} = (n_x, n_y)$ and it directs inward to the cylinder. Both cylinders are located at $(x_{c,k}, 0)$ ($k$=1, 2), respectively, when they are at rest in the calm water. The left and right cylinders are called as cylinders 1 and 2 respectively. The water bottom $S_{bot}$ is a plane at $y$=-$h$. As convenience for simulations, the fluid domain is truncated at an artificial boundary $S_c$, which is usually three- or four-times linear wavelength distance from the nearest cylinder. We denote $t$ as time and $\eta$ as wave elevation on free surface $S_f$. In the fluid domain $\forall$, the fluid is perfect, and its motion is irrotational. A velocity potential $\phi$ which satisfies the Laplace equation is introduced to describe the fluid motion

$$\nabla^2 \phi = 0 \qquad \text{in } \forall \,. \tag{1}$$

For flow problems with a uniform current with speed $U_0$ along the $x$-axis, the total velocity potential in the fluid domain is expressed as

$$\Phi = U_0 x + \phi \,, \tag{2}$$

where $\Phi$ is also governed by the Laplace equation. The boundary conditions should be imposed on all boundaries for solving the boundary value problem to obtain the potential. The potential $\phi$ is used in the simulation and its kinematic and dynamic conditions on the free surface $S_f$ can be written as

$$\left.\begin{aligned}\frac{Dx}{Dt} &= U_0 + \frac{\partial\phi}{\partial x}\\ \frac{Dy}{Dt} &= \frac{\partial\phi}{\partial y}\end{aligned}\right\}, \tag{3a, b}$$

$$\frac{D\phi}{Dt} = -g\eta + \frac{1}{2}\left|\nabla\phi\right|^2, \tag{4}$$

respectively, where $g$ denotes the gravity acceleration and $\frac{D}{Dt} = \frac{\partial}{\partial t} + \nabla\phi\cdot\nabla$ is the material derivative.

To satisfy the radiation condition, an artificial damping zone is placed near the truncated boundary $S_c$ to absorb the incoming wave and minimize the reflection. This is achieved through adding a damping term in Eqs. (3) and (4), or

$$\left.\begin{aligned}\frac{Dx}{Dt} &= U_0 + \frac{\partial\phi}{\partial x}\\ \frac{Dy}{Dt} &= \frac{\partial\phi}{\partial y} - \nu(x)y\end{aligned}\right\}, \tag{5a, b}$$

$$\frac{\mathrm{D}\phi}{\mathrm{D}t} = -g\eta + \frac{1}{2}\nabla\phi\nabla\phi - \nu(x)\phi, \tag{6}$$

where $\nu(x)$ denotes the artificially viscous coefficient and its expression in detail may be found in Wang et al. [13].

The impermeable condition on the cylinder surface can be expressed as

$$\frac{\partial\phi}{\partial n} = -U_0 n_x + \vec{n}\cdot(\vec{\mathrm{v}} + \vec{\Omega}\times\vec{r}) \qquad \text{on } S_b, \tag{7}$$

where $\vec{\mathrm{v}}$ is the translational velocity of cylinder 1 or 2 at $x = x_{c,k} (k=1,2)$ and $y = 0$, $\vec{\Omega}$ is the angular velocity around the axis $z_k$ which passes through $(x_{c,k}, 0)$ and is perpendicular to the *xoy* plane. $\vec{r} = (x - x_{c,k}, y)$ is the location vector.

On the bottom of the water, the velocity potential $\phi$ satisfies

$$\frac{\partial\phi}{\partial n} = 0 \qquad \text{on } S_{bot}. \tag{8}$$

The initial conditions including the position of the free surface and the potential on it are given as

$$\left.\begin{array}{l} y(t=0)=0 \\ \phi(x,y;t=0)=0 \end{array}\right\}. \tag{9a, b}$$

The velocity potential in the fluid domain is obtained through solving Eqs. (1), (5) ~ (9). The pressure on the cylinder surface is calculated by using the Bernoulli equation

$$p=-\rho(\frac{\partial\phi}{\partial t}+U_0\frac{\partial\phi}{\partial x}+\frac{1}{2}|\nabla\phi|^2+gy), \tag{10}$$

where $\rho$ denotes the fluid density. The hydrodynamic force and moment acting on the cylinder can be obtained by a direct integration of the pressure over the instantaneous wetted cylinder surface

$$\vec{F}_j=\int_{S_b} p\vec{n}_j ds. \tag{11}$$

In above equation, $\vec{n}_j=(n_1,n_2,n_3)=(n_x,n_y,n_z,r_xn_y-r_yn_x)$ is the normal vector of any point on the surface of cylinder, where ($r_x$, $r_y$) is the location vector. In Eq. (11), a problem is how to calculate the integral of $\partial\phi/\partial t$ or $\phi_t$ over the wetted body surface. Here, we choose to follow the procedure proposed in Wu [35] and Wu and Eatock Taylor [36]. Through introducing a term related to the uniform current in Eq. (2), this approach is now extended to forward speed problems or problems with current effects. In particular, the term $\phi_t$ satisfies the Laplace equation in the fluid domain as

$$\nabla^2\phi_t=0. \tag{12}$$

On the free surface, $\phi_t$ is obtained through

$$\phi_t=-gy-\frac{1}{2}\nabla\phi\nabla\phi-U_0\frac{\partial\phi}{\partial x} \quad . \tag{13}$$

On the stationary boundary, $\phi_t$ satisfies

$$\frac{\partial\phi_t}{\partial n}=0, \tag{14}$$

and on the nonstationary boundary, it is

$$\frac{\partial \phi_t}{\partial n} = (\dot{\vec{\mathrm{v}}} + \dot{\vec{\Omega}} \times \vec{r}) \cdot \vec{n} - \vec{\mathrm{v}}.\frac{\partial \nabla \phi}{\partial n} + \vec{\Omega} \cdot \frac{\partial}{\partial n}\{\vec{r} \times [(\vec{\mathrm{v}} - \vec{U}_0) - \nabla \phi]\}, \tag{15}$$

where the dot over $\vec{\mathrm{v}}$ and $\vec{\Omega}$ means the derivative with respect to time. Thus, the time derivative $\phi_t$ can be obtained through solving Eqs. (12) ~ (15).

## 3. FINITE ELEMENT DISCRITAZATION AND NUMERICAL PROCEDURES

In the present simulations, we employed a finite element method with 8-node quadrilateral isoparametric element (see Fig. 2) to calculate the velocity potential at each time step. The shape functions defined in a local coordinate system $\vec{\xi} = (\xi, \zeta)$ corresponding to element *e* with eight nodes may be expressed as

$$\left.\begin{aligned} N_i^{(e)}(\xi,\zeta) &= \frac{1}{4}(1+\xi_i\xi)(1+\zeta_i\zeta)(\xi_i\xi+\zeta_i\zeta-1) \quad && (i=1,2,3,4) \\ N_i^{(e)}(\xi,\zeta) &= \frac{1}{2}(1-\xi^2)(1+\zeta_i\zeta) && (i=5,7) \\ N_i^{(e)}(\xi,\zeta) &= \frac{1}{2}(1-\zeta^2)(1+\xi_i\xi) && (i=6,8) \end{aligned}\right\}. \tag{16a, b, c}$$

The Evaluation of first and second order derivatives of potential with respect to coordinates such as $\partial\phi/\partial x$, $\partial\phi/\partial y$, $\partial^2\phi/\partial x^2$ ,$\partial^2\phi/\partial x\partial y$ and $\partial^2\phi/\partial y^2$ , which are required in Eqs. (5), (6), (10) and (15) can be obtained through differentiating the shape functions or Eq. (16) directly. The Detailed finite element discretization and calculation of derivatives can be found in Wang et al. [13]. The element coefficient matrices can be calculated in every quadrilateral element, and they are then assembled into a global coefficient matrix **M**. Meanwhile, the right-hand side vector **F** with considering the normal velocity on the boundary can also be calculated. Thus, a system of linear equations by finite element method can be established as

$$\mathbf{M\Phi} = \mathbf{F}, \tag{17}$$

where $\mathbf{\Phi} = [\phi_1, \phi_2, \cdots, \phi_n]^T$ is the velocity potential vector containing potentials $\phi_i (i = 1,2,\cdots,n)$ and *n* is the total number of nodes in the discretized fluid domain. Eq. (17) can be solved through the conjugate gradient method with a symmetric successive overrelaxation (SSOR) preconditioner.

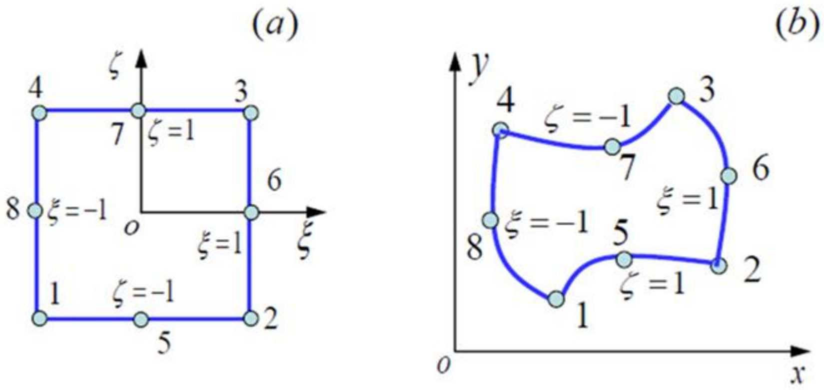


**Fig. 2.** 8-node quadrilateral isoparametric element.

On the free surface, nodes ($x_i$, $y_i$) ($i$=1,2,..,$n$) and their potential $\phi$ at the next time step are calculated through Eqs. (5) ~ (6), which is numerically implemented based on the fourth-order Runge-Kutta method. It should be noticed that the intersection points between the free surface and the cylinder surface should be handled because very small gap exists between them in the simulation and the closest nodes to the cylinder surface should be taken back to stay on the cylinder surface at each time step. Furthermore, the nodes ($x_i$, $y_i$) ($i$=1,2,..,$n$) should be redistributed every several time steps to avoid clustering or stretching, and the redistribution will be performed more frequently due to the existence of the current speed than that without current. In addition, a remeshing method based on the B-spline function [37] is applied for smoothing the free surface during the simulation.

## 4. NUMERICAL RESULTS

We consider twin rectangular cylinders in vertical or horizontal oscillations. Wang et al. [13] made simulations of fully nonlinear wave motions between twin rectangular, wedged-shaped and elliptical cylinders in specified oscillations without current. They found that the resonance is much more serious in the rectangular cylinder than those for the wedge-shaped and elliptical cylinders. Thus, we investigate two rectangular cylinders in forced oscillations only in the present paper. Besides, the effect of a uniform current is further considered. The width of each cylinder is 2$b$ and the initial draught is $d$=$b$/2 at still water plane. The still water depth $h$=10$d$. The spacing between the centre lines of the two cylinders is denoted by $l_c$. Cylinders 1 and 2 are initially located at $x_{c,1}$=-$l_c$/2 and $x_{c,2=}l_c$/2, respectively.

The cylinders are subject to following oscillation in vertical or horizontal direction

$$\delta = A\sin\omega t\ , \tag{18}$$

where $A$ is the oscillational amplitude and $\omega$ is the oscillational frequency. A modulation function is applied in Eq. (7) [12] to ensure the wave developing gradually and smoothly. The current speed $U_0$ is nondimensionalized as the Froude number and it is defined as $F_n = U_0/\sqrt{gb}$. As discussed in Wang and Wu [12] based on the second-order theory, the real resonant frequency is

$$\omega_i' = C_i\omega_i\ (i = 1,2,\cdots) \tag{19}$$

for cases without current, where $C_i$ is a constant and can be obtained by numerical tests. $\omega_i$ is defined as

$$\omega_i = \sqrt{\frac{i\pi}{l_c - b}g}, \quad (i = 1,2,...)\ , \tag{20}$$

and it is the resonant or natural frequency of a sloshing container with ($l_c$-$b$) in width and great depth of water. It should be noted that the resonant frequency is equal to the oscillational frequency predicted by Eq. (19) of both cylinders when resonance happens at $F_n$=0. However, they are somewhat different from each other when a current exists. For convenience, the oscillational frequencies corresponding to the real resonant frequencies $\omega_i'\ (i = 1,2,...)$ are denoted as $\omega_i''(i = 1,2,...)$ here when $F_n \neq 0$.

**4.1. Wave resonance induced by vertical motions of the cylinder**

We first make some simulations at $A/d$=0.0125 for both cylinders in a completely same vertical motions at three Froude numbers $F_n$=0, 0.064 and 0.128. The spacing between two cylinders is chosen as $l_c$=8$b$. The situation of a current propagating along the negative $x$-direction or $F_n$<0 is not considered here due to the symmetric properties of the problem. Besides, the waves between two cylinders are generally much larger than those outside the cylinders at resonant frequencies [12, 13]. Thus, we may pay more attention to the regions between two cylinders. For convenient comparison, we may denote the positions of the left and right sides of cylinder 1 by $p_{l1}$ and $p_{r1}$, while using $p_{l2}$ and $p_{r2}$ for cylinder 2. Fig. 3 gives the nondimensionalized values of maximum wave elevations $\eta_{\max}$ at $p_{r1}$ & $p_{l2}$ versus the nondimensionalized oscillational frequency $\omega/\omega_2$, where $\omega_2$ is defined in Eq. (20). At $F_n$=0 (see Fig. 3a), the two curves coincide with each other because of symmetry, and their three peaks at $\omega/\omega_2$=0.505, 1.001 & 1.413 approximately can be observed. Among them, the maximum wave is at $\omega/\omega_2$=1.001, while that at $\omega/\omega_2$=0.505 is the smallest and an enlarged view is given to show. As discussed by Wu [1], Wang and Wu [12] and Wang et al. [13], for symmetric motions such as vertical oscillations in an identical direction or horizontal oscillations in opposite directions. The first- and second-order resonances happen at the even order resonant frequencies $\omega_{2i}(i=1,2,...)$ and half of the even order resonant frequencies $\omega_{2i}/2(i=1,2,...)$, respectively. By contrast, when the system undergoes asymmetric motions such as the horizontal oscillations toward an identical direction, the first-order resonance happens at $\omega_{2i-1}(i=1,2,...)$, while the second-order resonance is at $\omega_{2i}/2(i=1,2,...)$. For the case without the current or $F_n$=0, only little differences between the fully nonlinear results and second-order solution are observed. In particular, the second-order resonance actually happens at $\omega/\omega_2 = 0.5\omega_2''/\omega_2 \approx$0.505, which is very close to the prediction value $\omega/\omega_2$ =0.5, while the first-order resonance happens at $\omega/\omega_2 = \omega_2''/\omega_2$=1.001 and $\omega/\omega_2 = \omega_4''/\omega_2$=1.413, which is very close to and $\omega_2/\omega_2$=1 and $\omega_4/\omega_2 = 1.414$ predicted by Eq. (20).

Figs. 3b gives the maximum waves at $F_n$=0.064. Compared with $F_n$=0 in Fig. 3a, a distinct difference is that two peaks appear at $\omega_1''/\omega_2$=0.753 and $\omega_3''/\omega_2$=1.217, which are close to the anti-symmetrical resonance frequencies $\omega_1/\omega_2$=0.707 and $\omega_3/\omega_2 = 1.225$ predicted by Eq. (20). The reason why two peaks appear at $\omega_1''/\omega_2$=0.753 and $\omega_3''/\omega_2$=1.217 is probably that the fluid motion becomes asymmetric due to the presence of the current and hence the resonances around the odd-order frequencies $\omega'_{2i-1}(i=1,2)$ can be observed. Besides, the nondimensionalized oscillational frequencies $0.5\omega''_2/\omega_2$ and $\omega''_i/\omega_2\ (i=2,4)$ become slightly smaller and change from 0.505, 1.001 & 1.413 at $F_n$=0 to 0.502, 0.998 & 1.403 at $F_n$=0.064, respectively. Another interesting phenomenon can be noticed is that both the peaks at $\omega''_2/\omega_2$=0.998 and $\omega''_4/\omega_2$=1.403 in Fig. 3b become smaller when comparing with the corresponding ones in Fig. 3a, respectively. When the Froude number continue to increase to 0.128 (see Fig. 3c). It can be seen that the peak at around $0.5\omega''_2/\omega_2=0.5$ almost disappears, and even that at $\omega''_4/\omega_2$ cannot be graphically seen. The oscillational frequencies $\omega''_1/\omega_2$, $\omega''_2/\omega_2$ and $\omega''_3/\omega_2$ become more smaller and they are 0.747, 0.988 & 1.194, respectively. Furthermore, it can be seen that peak at $\omega''_1/\omega_2$=0.747 and $\omega'_3/\omega_2$=1.193 clearly become larger than those at $F_n$=0.064. In summary, all oscillational frequencies $\omega''_i(i=1,2,3,4)$ slightly decrease as the increases of $F_n$. The peak at $\omega''_i/\omega\,(i=2,4)$ decline and that at $\omega''_1/\omega\,(i=1,3)$ increase as the increase of $F_n$, respectively.

Fig. 4 gives a clearer comparison of maximum wave elevation at $p_{r1}$. The main peaks at $\omega''_2$ are around 39.45, 37.97 and 34.65 at $F_n$=0, 0.064 and 0.128, respectively, which means the wave peak at resonance generally decreases as the Froude number increases. Similar declination is also observed at $\omega''_4$. However, the situation here is a little different. The peak at $F_n$=0.128 is the least obvious but its magnitude is larger than that at $F_n$=0.064. This is because the resonance effect at $\omega''_4$ is not as strong as that at $\omega''_2$. When a current with larger speed exists, the current effect may dominate the wave-current-structure interactions and weaken the resonance. In such a case, the waves at the intersection points between the free surface and the cylinder surface will be mainly evaluated by the current. By contrast, the peaks around $\omega''_1$ and $\omega''_3$ clearly increases as the increases of the Froude number, which indicates the current can reduce the resonant effect at $\omega''_2$ and $\omega''_4$ but enhance that at $\omega''_1$

and $\omega_3''$. Besides, the phenomenon at $\omega_2''/2$ is similar to that at $\omega_4''$. Fig. 5 shows the corresponding maximum horizontal forces $F_{x,\max}$ on both cylinders versus the nondimensionalized frequency, which is generally similar to the wave depicted in Fig. 4.

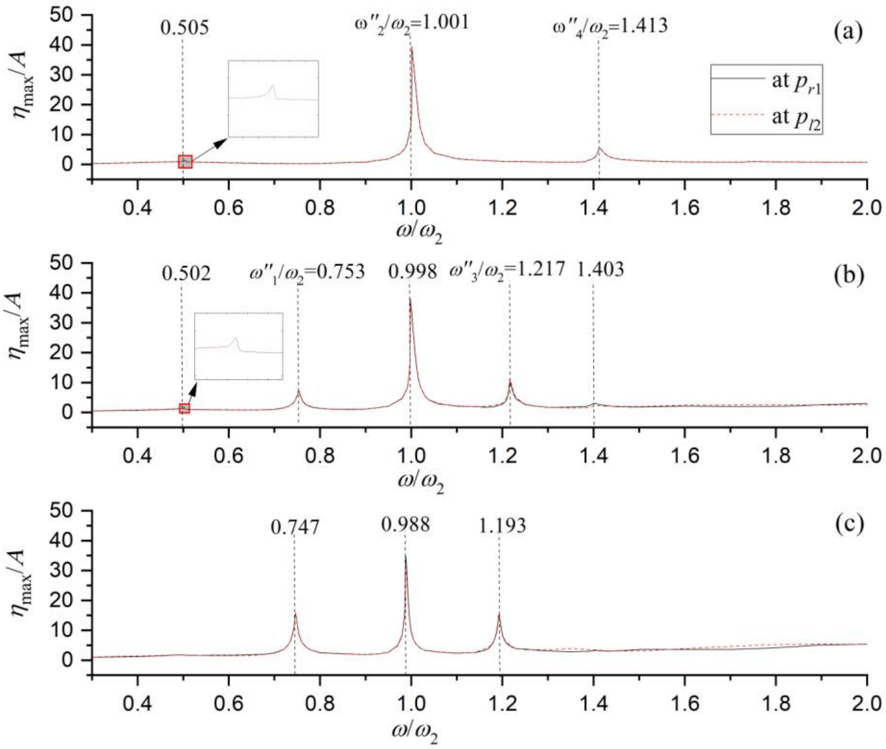


**Fig. 3.** Maximum values of waves versus $\omega/\omega_2$; (a) $F_n$=0; (b) $F_n$=0.064; (c) $F_n$=0.128.

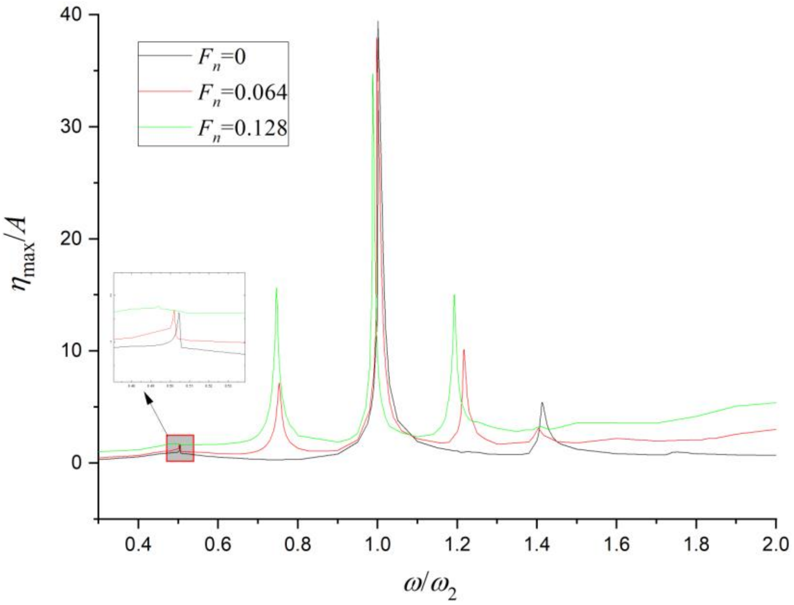


**Fig. 4.** Maximum values of waves at $p_{r1}$ versus $\omega/\omega_2$.

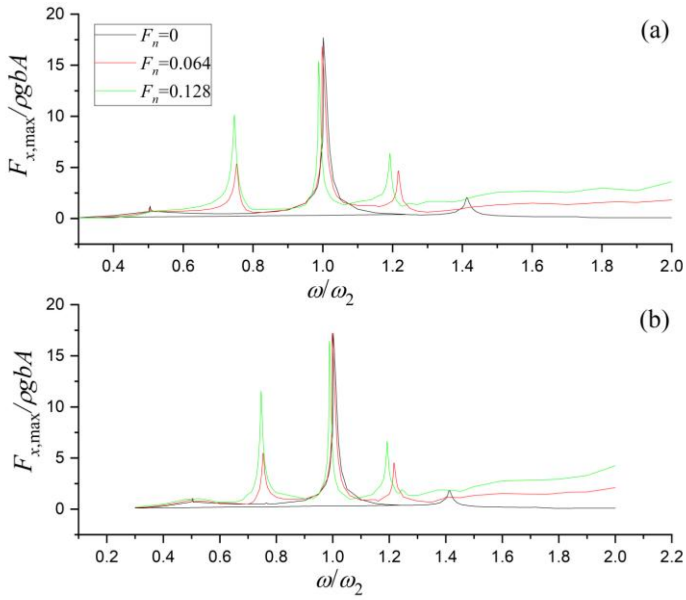


**Fig. 5.** Maximum horizontal forces on (a) cylinder 1 and (b) cylinder 2 versus $\omega/\omega_2$.

Fig. 6 shows convergence tests for mesh and time interval. In the figure, $\eta$ expresses the wave elevation. Wang et al. [13] have tested the cases at $F_n$=0 and hence we give convergence tests at $F_n$=0.128 only. The test of waves at $p_{r1}$ & $p_{l2}$ is at $\omega_2''/\omega_2$=0.988, which is the position of the main peak. The control surfaces $S_c$ at both ends are located at distance about four times wavelength away the nearest cylinder. Two meshes and time intervals are used to test the numerical convergence. The details are given in Table 1, where NF1 is the segment number along the free surface on the left of cylinder 1 or the right of cylinder 2, NF2 denotes the segments on the free surface between the two cylinders, ND and NB denote the segments along the vertical and horizontal faces of each cylinder respectively, NH represents the segment on the both control surfaces $S_c$ at the far ends, NE and NN are the total numbers of elements and nodes in the whole fluid domain respectively. The results for Case 1 and Case 2 are given in Fig. 6. It can be seen that they are in very good agreement over the entire simulations of two hundred cycles. These tests show that Case 1 with 3904 elements & 12201 nodes and $\Delta t = T/250$ can provide convergent results in this case.

Table 1. Parameters of mesh schemes

| | NF1 | NF2 | ND | NB | NH | NE | NN | $\Delta t$ |
|---|---|---|---|---|---|---|---|---|
| Case 1 | 70 | 42 | 9 | 12 | 20 | 3904 | 12201 | T/250 |
| Case 2 | 100 | 60 | 14 | 18 | 26 | 7192 | 22277 | T/500 |

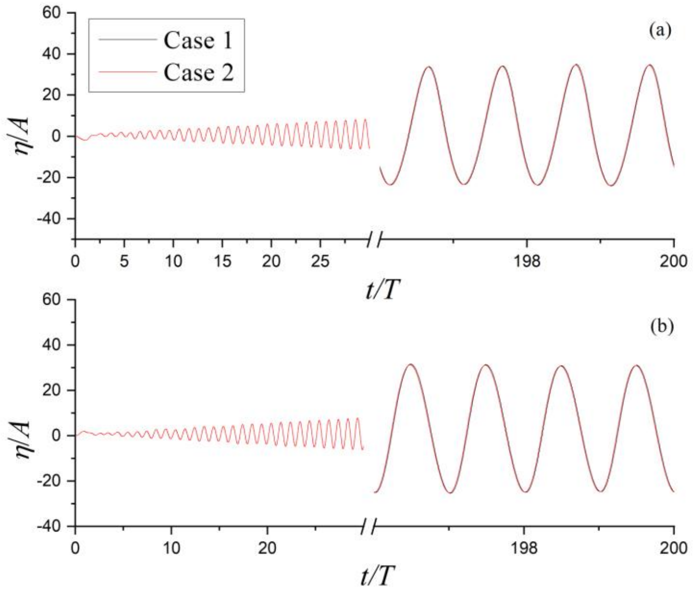


**Fig. 6.** Comparisons of waves with different meshes and time intervals at $F_n$=0.128. (a) at $p_{r1}$; (b) at $p_{l2}$.

Fig. 7 gives wave histories at $p_{r1}$ and $p_{l2}$ at the nondimensionalized oscillational frequencies $\omega_2'' / \omega_2$. Similar variation trends can be observed in these three waves at both $p_{r1}$ and $p_{l2.}$ In particular, the amplitude generally increases as the development of most time and then a gradual decline may appear at the end of simulation time. It has already been shown in Fig. 4 that the maximum wave within the simulation time of two hundred cycles clearly decreases as the increase of $F_n$ at $\omega_2'' / \omega_2$. The wave histories in this figure show how the waves develop as the increase of time at the resonant frequencies and the three Froude numbers, and this is distinctly different from the situation of a single cylinder shown in Fig. 8, in which the wave runup rises to a bigger value as the increase of $F_n$ at both the left and right sides. Moreover, the wave runup in Fig. 7 are much larger than those in Fig. 8, in which the waves runups at $F_n$=0, 0.064 and 0.128 are about 0.6, 0.88 & 1.83 at the right side and 0.6, 0.97 & 1.89 at the left side, respectively.

A comparison of wave between the fully nonlinear results and the linear plus second order solutions at $\omega_2'' / \omega_2 = 1.001$ and $F_n$=0 is given in Fig. 9. Detailed simulations of wave resonance due to oscillations of two rectangular cylinders in a current based on the second order theory can be found in Huang and Wang [33]. It can be seen from the figure that the nonlinear wave is in good agreement with the linear plus second order solution within the first forty cycles and then they become distinctly discrepant. It should be mentioned that the above three resonant frequencies are a little different from those obtained by Huang and Wang [33] and it is because the former is based on the fully nonlinear model and the latter is on the second order theory. In particular, according to the second order theory [33], the nondimensionalized oscillational frequencies $\omega_2''/\omega_2$ at $F_n$=0, 0.064 & 0.128 are about 1.01, 1.005 & 0.99, respectively. In the case of $F_n$=0, the wave histories at $p_{r1}$ are given in Fig. 10 with $\omega_2''/\omega_2 = 1.01$ and it is shown that the linear and linear plus second-order waves always increase as the time, but the fully nonlinear wave has a clear envelope oscillating at a lower frequency and it maximum peak is much smaller than those of linear and linear plus solution solutions. Thus, the waves exhibit a completely different change at the two frequencies $\omega_2''/\omega_2 = 1.001$ and 1.01, which are calculated based on the fully nonlinear model and the second order theory, respectively. Similarity can be found for the waves at $F_n$=0.064, which is not given here. Further comparison of wave at $p_{r1}$ at resonant frequency $\omega_2''/\omega_2 = 0.988$ and at $F_n$=0.128 is given in Fig. 11. The waves are in good agreement between the fully nonlinear result and the linear plus second order solution before $t/T$=25.

Fig. 12 shows the corresponding hydrodynamic forces on cylinder 1 at $\omega_2''/\omega_2 = 1.001$, 0.998 & 0.988 at $F_n$=0, 0.064 & 0.128, respectively. The variation of the horizontal force $F_x$ with the Froude number is similar to that of the wave. It is also noted that all vertical components $F_y$ at smaller Froude number have more evident double peaks, which corresponds to stronger nonlinear feature.

Fig. 13 shows histories of waves at $p_{r1}$ with $A/d$=0.0125, 0.025 and 0.05. It can be seen that the difference between the three nondimensionalized waves at each $F_n$ is very clear. Generally, the wave nonlinearity becomes stronger as the amplitude increases at each $F_n$. However, as pointed out by Wang et al. [13] that the waves in smaller oscillational amplitudes can exhibit clearer resonant behaviour because their nondimensionalized amplitudes are larger. In other words, the wave resonances in larger oscillational amplitudes are weaker.

Fig.14 depicts the wave profiles from $t$=196$T$ to 200$T$ with a time interval $\Delta t$ =0.1$T$ at

$\omega_1''$ and $\omega_2''$ with the aforementioned three Froude numbers. It is known that no resonance happens at $\omega_1''$ when $F_n$=0 (see Fig. 14a). We then replace $\omega_1''$ with $\omega_1$ obtained by Eq. (20) for comparisons with those at $\omega_1''$ when $F_n$=0.064 & 0.128. It is seen that the wave between the two cylinders is much larger than those outside the two cylinders except that in Fig. 14a. The wave development with time can be also clearly seen and differences between different $F_n$ can also be observed.

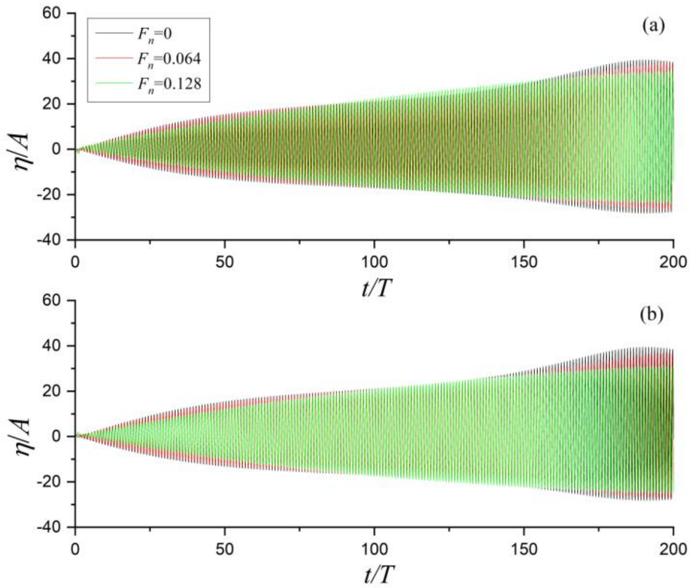


**Fig. 7.** Histories of waves at oscillational frequencies $\omega_2''$; (a) at $p_{r1}$; (b) at $p_{l2}$.

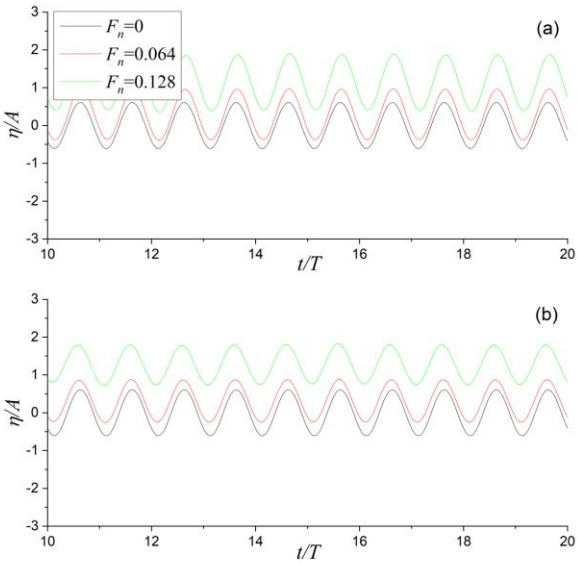


**Fig. 8.** Histories of waves at (a) the right side and (b) the left side of a single cylinder at $\omega_2''$.

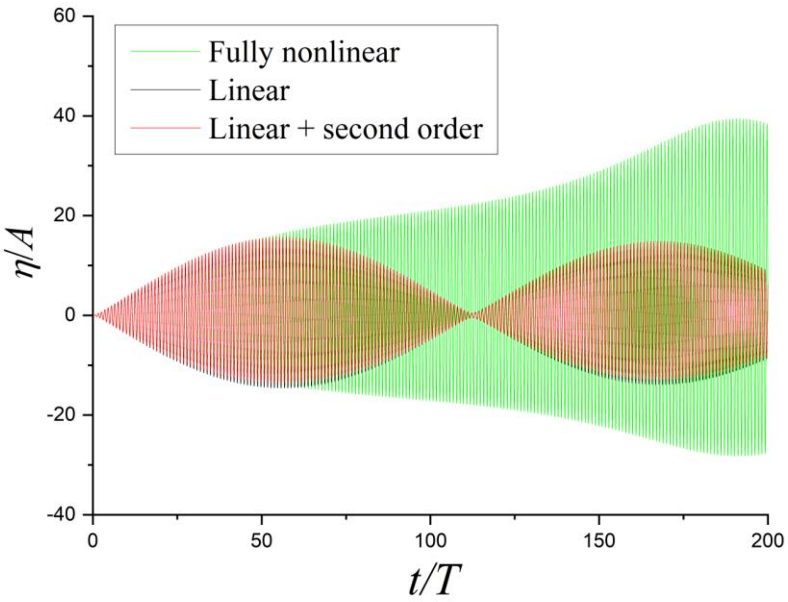


**Fig. 9.** A comparison of waves with linear and linear plus second order solutions at $\omega_2'' / \omega_2 = 1.001$ & $F_n$=0.

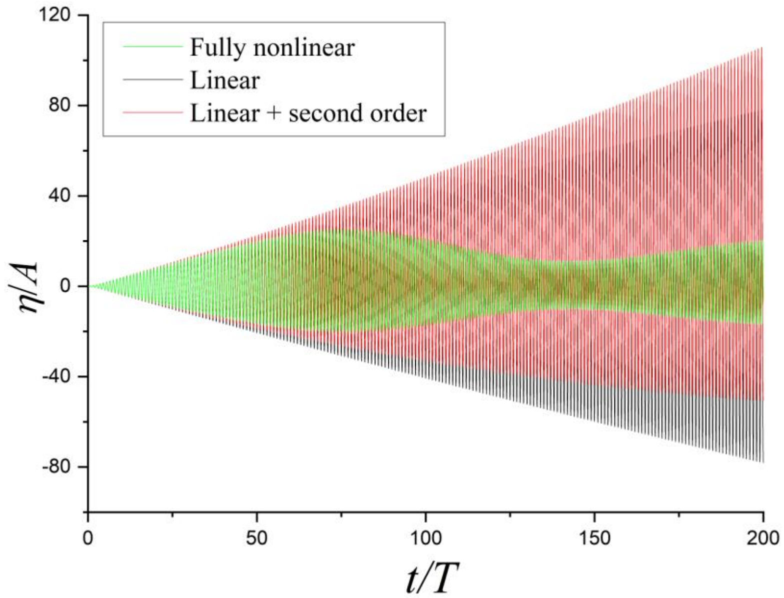


**Fig. 10.** Comparisons of waves with linear and linear plus second order solutions at $\omega_2'' / \omega_2 = 1.01$ & $F_n$=0.

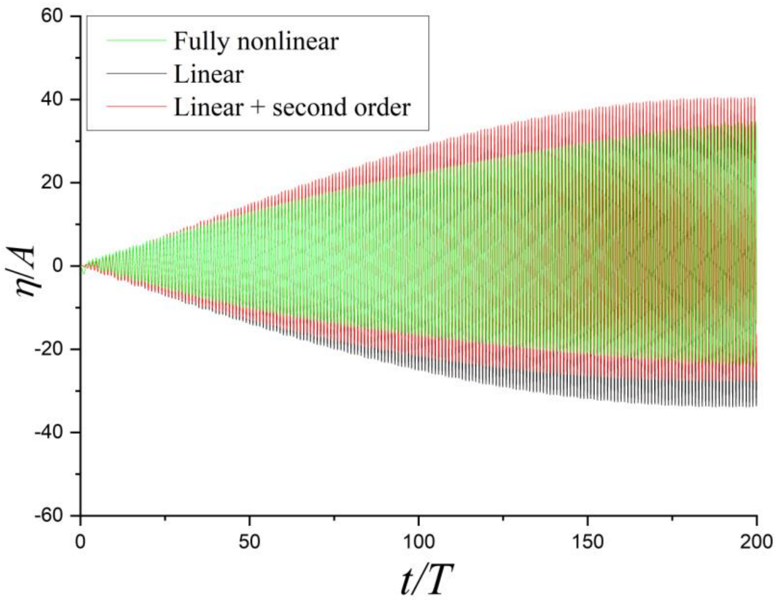


**Fig. 11.** Comparisons of waves with linear and linear plus second order solutions

at $\omega_2''/\omega_2 = 0.988$ & $F_n$=0.128.

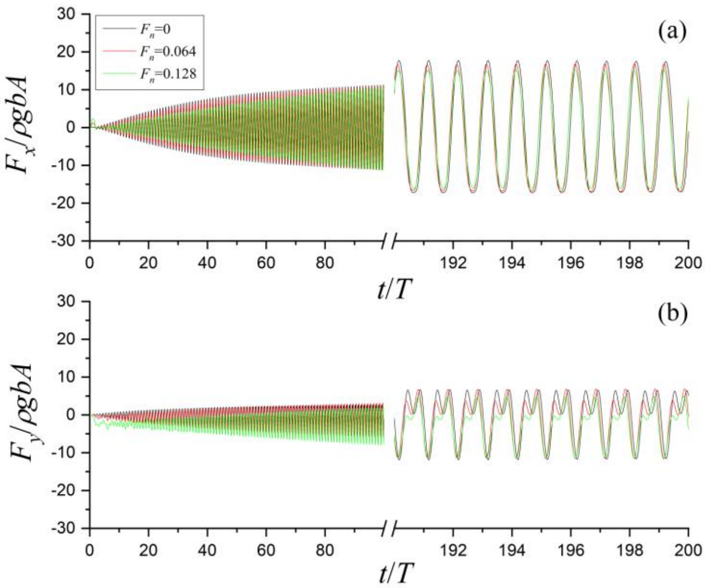


**Fig. 12.** Histories of forces on cylinder 1 at $\omega_2''$.

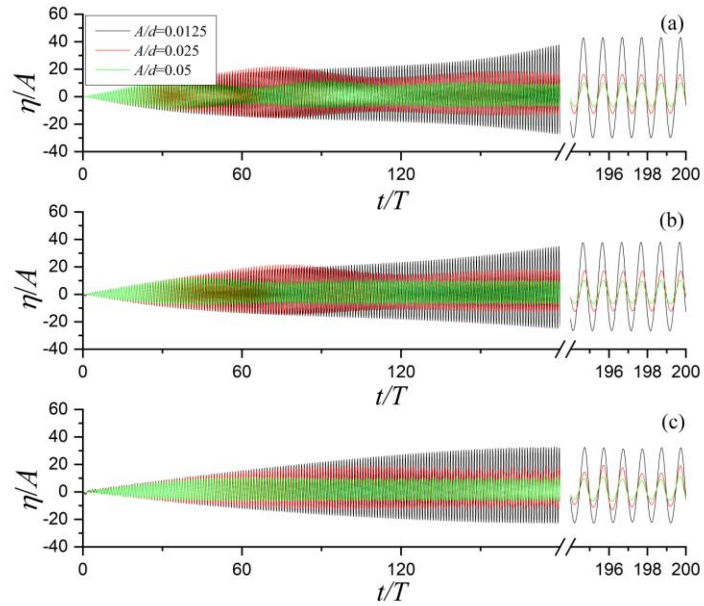


**Fig. 13.** Histories of waves at $p_{r1}$ at $\omega_2''$; (a) $F_n$=0; (b) $F_n$ =0.064; (c) $F_n$ =0.128.

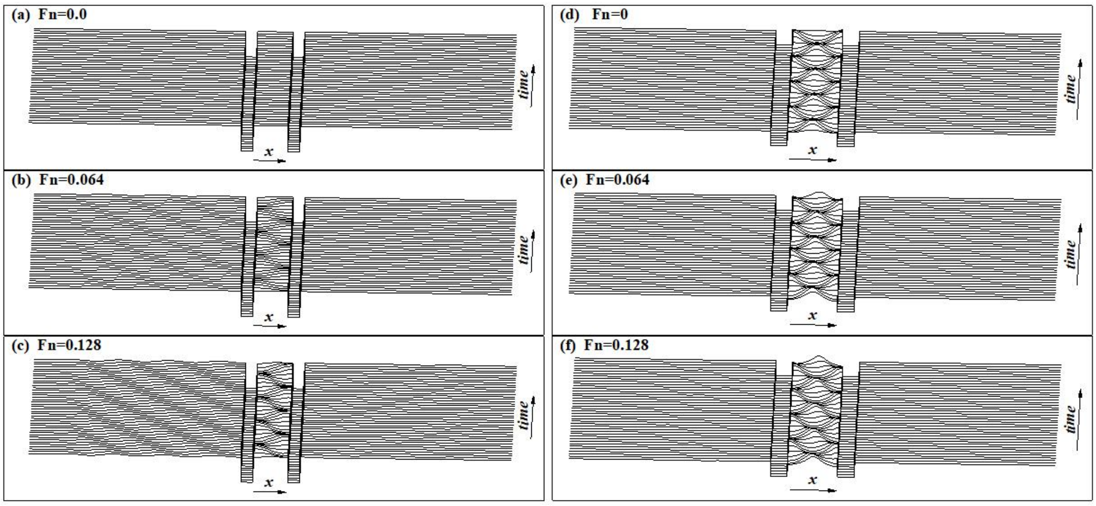


**Fig. 14.** Snapshots of wave profiles at (a), (b) & (c) $\omega = \omega_1''$ and (d), (e) & (f) $\omega = \omega_2''$ from $t$=196$T$ to 200$T$ with time interval $\Delta t$ =0.1$T$.

The work mentioned above is for the spacing between two cylinders $l_c$=8$b$. In fact, the resonance behaviour is also affected by the ratio $l_c/b$. We also made simulations at different $l_c/b$ from 5 to 9 besides $l_c/b$=8. We first give the results of maximum waves and forces versus $l_c/b$ at $\omega_2''$ in Fig. 15. It can be seen that both the wave peaks and force peaks at three different $F_n$ increase as $l_c/b$. Besides, for a given $l_c/b$, the maximum waves and forces also increase with $F_n$. Similar analyses are also conducted for the results at $\omega_1''$ and $\omega_3''$, which are depicted in Fig. 16. It should be noted that only the situations at $F_n$=0.064 & 0.128 are provided due to no resonance or no peak at $F_n$=0. It is clearly shown that both maximum waves and forces at every $l_c/b$ become larger when $F_n$ increase from 0.064 to 0.128. However, for a given $F_n$, the maximum waves and forces at $\omega_1''$ and $\omega_3''$ do not just show a increase trends as those at $\omega_2''$.

The nondimensionalized frequencies $\omega_1''/\omega$ , $\omega_2''/\omega$ , $\omega_3''/\omega$ and $\omega_{2\mathrm{h}}''/\omega$ versus the spacing $l_c/b$ is given in Fig. 17, in which $\omega_{2\mathrm{h}}''$ is the oscillational frequency at the second order resonance and it is approximately half of $\omega_2''$ in the case of $l_c/b$=8. It can be seen that all resonant frequencies generally become smaller as $F_n$ increases at every $l_c/b$. $\omega_1''/\omega_2$ almost linearly increases as $F_n$ increases. However, both $\omega_{2\mathrm{h}}''/\omega_2$ and $\omega_3''/\omega_2$ rise quickly in the beginning and then have a slight change as the increase of $l_c/b$. The situation at $\omega_2''/\omega_2$ is similar to the linear solutions presented in Huang and Wang [33]. It is also noticed that $\omega_{2\mathrm{h}}'' \approx \omega_2''/2$ at larger $l_c/b$. However, the discrepancy between $\omega_{2\mathrm{h}}''$ and $\omega_2''/2$ is more evident at smaller $l_c/b$. For example, as shown in Fig. 18, $\omega_{2\mathrm{h}}''$ at all three $F_n$ are around 0.41 at $l_c/b$=5, which is quite different from the corresponding value of $\omega_2''/2$ . This is probably due to the evident effects of narrower spacings on the lower frequency waves when resonance happens.

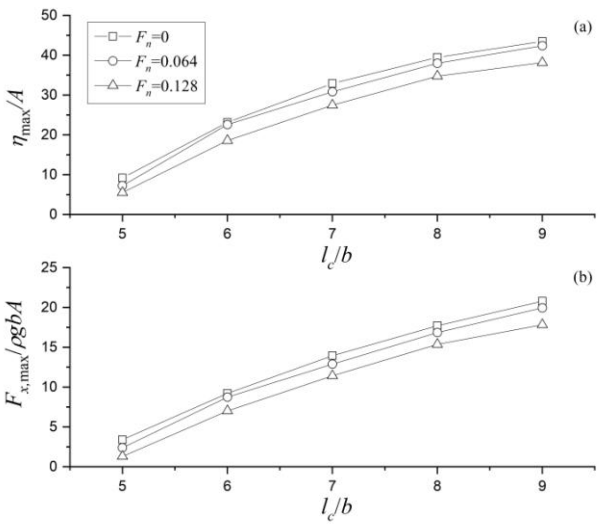

**Fig. 15.** Maximum waves and horizontal forces versus $L_{cy}/b$ at $\omega_2''$; (a) waves at the right side of cylinder 1; (b) horizontal forces on cylinder 1.

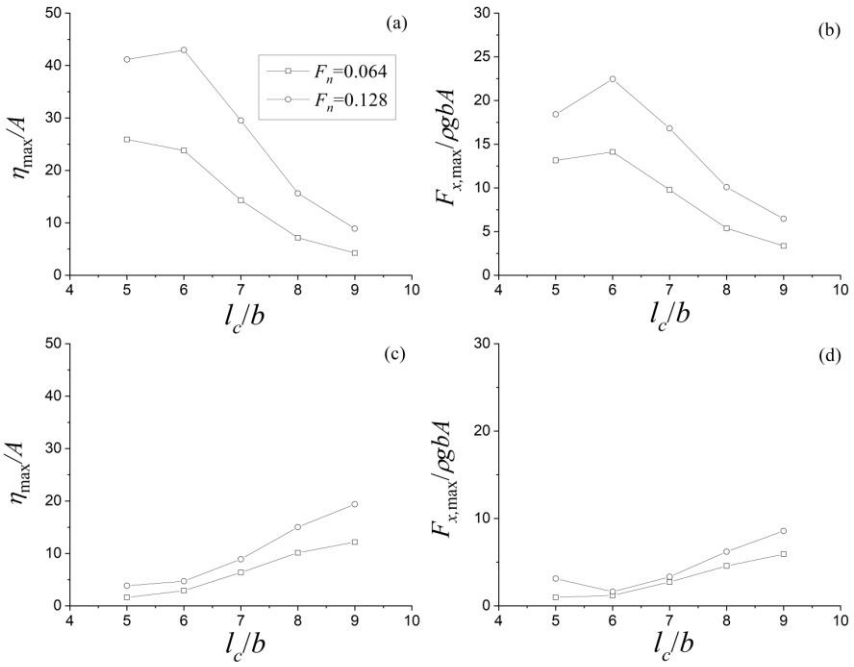


**Fig. 16.** Maximum waves and horizontal forces versus $l_c/b$; (a) waves at $p_{r1}$ at $\omega_1''$; (b) horizontal forces on cylinder 1 at $\omega_1''$; (c) waves at $p_{r1}$ at $\omega_3''$; (d) horizontal forces on cylinder 1 at $\omega_3''$.

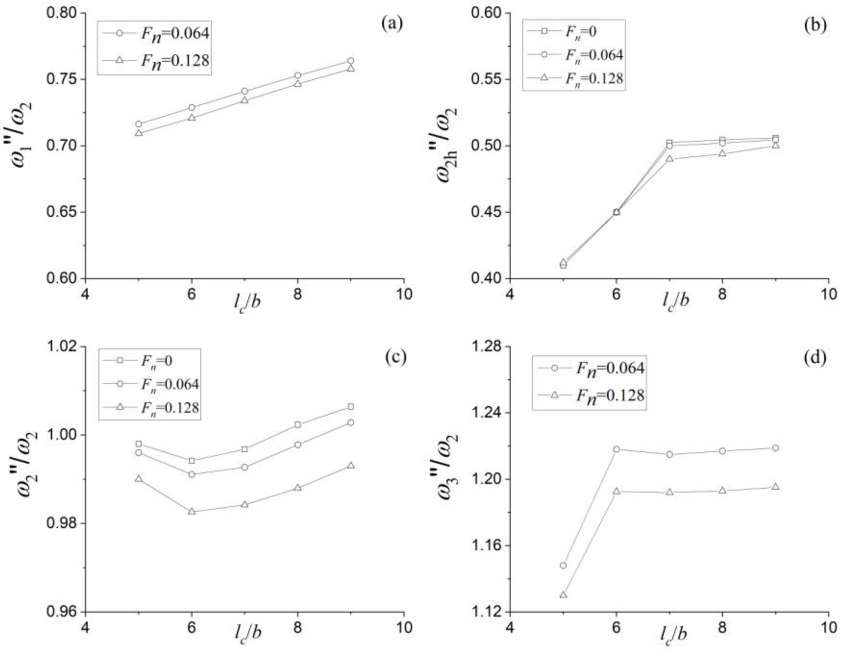


**Fig. 17.** Resonant frequencies versus $l_c/b$.

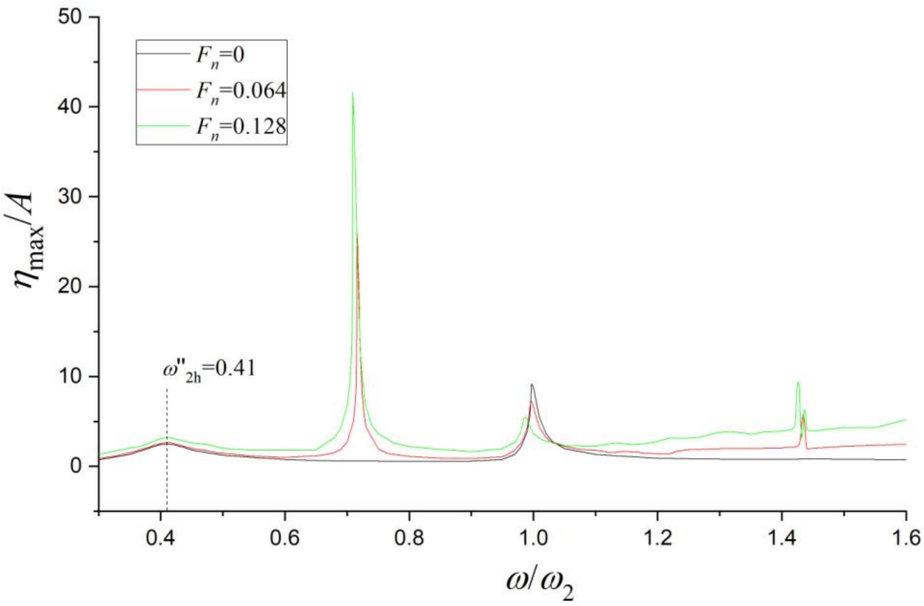


**Fig. 18.** Maximum values of waves at $p_{r1}$ versus $\omega/\omega_2$ at $l_c/b$=5.

Fig. 19 gives the waves versus $\omega/\omega_2$ at $A/d$=0.0125 and 0.05 to show the nonlinearity at different resonant frequencies. The maximum wave elevations clearly decline as the increase of $F_n$ at $\omega_1''/\omega_2$, $\omega_3''/\omega_2$ and $\omega_2''/\omega_2$, which is in agreement with the results given in Fig. 13. Furthermore, it is seen that each value of $\omega_1''/\omega_2$, $\omega_2''/\omega_2$ or $\omega_3''/\omega_2$ generally becomes a little smaller with the increase of $F_n$, and a comparison of values of oscillational frequencies $\omega_i''/\omega_2\ (i=1,2,3)$ at $A/d$=0.0125 and 0.05 in detail is given in Table 2. All these indicate that stronger nonlinearity and weaker resonant characteristic for waves in larger amplitudes. Similar phenomenon can be also observed in the hydrodynamic forces on cylinder 1 given in Fig. 20.

It is known that the fully nonlinear results obtained by the velocity potential theory may overpredict the results than those by experiments or simulation based on viscous flow theory. Thus, it may cause dispute that whether the velocity potential theory is suitable for simulations of wave resonance or not. As mentioned in Isaacson and Cheung [38], if the Keulegan-Carpenter number $K$ is less than 3, the flow separation effect is relatively localized and need not be considered, the potential theory is still valid. The Keulegan-Carpenter number $K$ is defined as

$$K=\pi A_e/D \tag{21}$$

whre $D$ is the characteristic diameter of body and $A_e$ the excursion amplitude of fluid particle. In our simulation, $D$=2$b$=2$m$ is the width of each cylinder, $A_e$ should be less than the maximum peaks.

Two maximum nondimensional peaks $\eta_{max}/A$ in Fig.19 are at $F_n$=0 and $\omega_2''$ and they are around 39.5 at $A/d$=0.0125 and 17.9 at $A/d$=0.05 (see Fig. 19a), and we replace $A_e$ with $\eta_{max}$ and substitute them into Eq. (21) and obtain their Keulegan-Carpenter number $K$ are 0.77 and 1.41, respectively, which are both less than 3. Hence, the aforementioned simulations are valid.

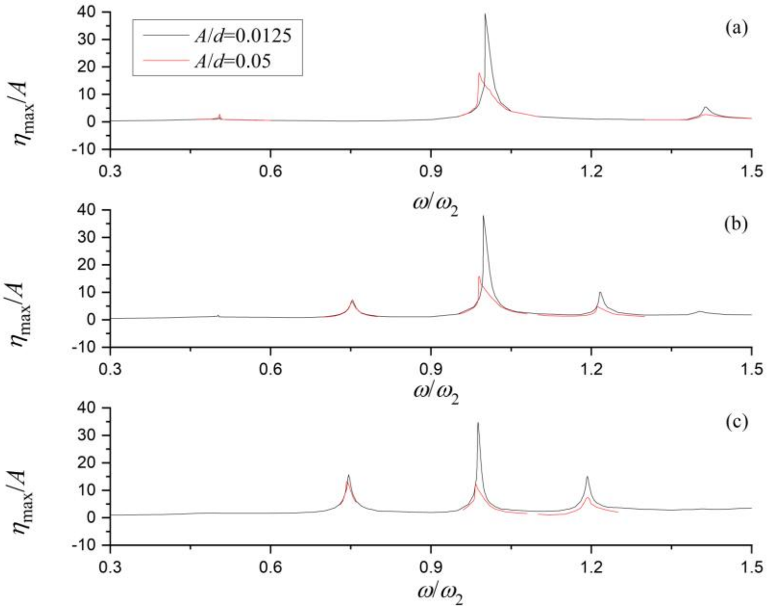


**Fig. 19.** Comparisons of maximum values of waves at $p_{r1}$ versus $\omega/\omega_2$ at $A/d$=0.0125 & 0.05; (a) $F_n$=0; (b) $F_n$=0.064; (c) $F_n$=0.128.

Table 2 The best approximations for $C_i = \omega_i''/\omega_2\ (i=1,2,3)$

| | $A/d$ | $\omega_1''/\omega_2$ | $\omega_2''/\omega_2$ | $\omega_3''/\omega_2$ |
|---|---|---|---|---|
| $F_n$=0 | 0.0125 | – | 1.001 | – |
| | 0.05 | – | 0.990 | – |
| $F_n$=0.064 | 0.0125 | 0.7530 | 0.998 | 1.217 |
| | 0.05 | 0.753 | 0.990 | 1.212 |
| $F_n$=0.128 | 0.0125 | 0.747 | 0.988 | 1.193 |
| | 0.05 | 0.743 | 0.984 | 1.193 |

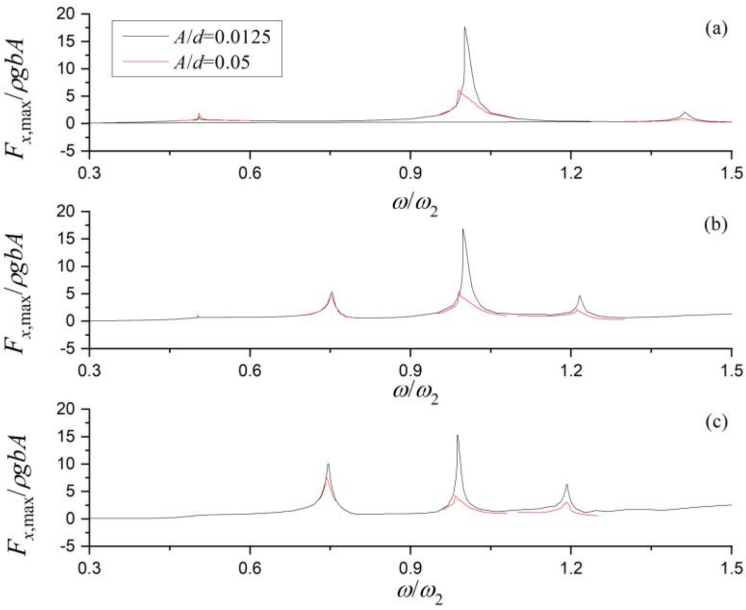


**Fig. 20.** Maximum horizontal forces on (a) cylinder 1 versus $\omega/\omega_2$ at $A/d$=0.0125 & 0.05; (a) $F_n$=0; (b) $F_n$=0.064; (c) $F_n$=0.128.

### 4.2. Wave resonance induced by horizontal motions of the cylinder

In addition to wave resonance induced by vertical motions of the cylinder, the resonances by horizontal motion of two cylinders in an identical direction given in Eq. (18) are also analysed here. The case at $l_c/b$=8 is first considered. Fig. 21 gives the maximum wave at $p_{r1}$ and the horizontal force on cylinder 1 versus $\omega/\omega_1$ at $A/d$=0.0125 & $F_n$=0. It is shown that three peaks for waves or forces can be clearly seen at $\omega/\omega_1 = \omega_i''/\omega_1\ (i=1,3,5) = 1.060$, 1.705 and 2.230, respectively, which are quite close to $\omega_i/\omega_1\ (i=1,3,5)$ predicted by Eq. (20) and they are 1.0, 1.732 and 2.236, respectively. As discussed by Wang and Wu [12], the first- and second-order resonances should have occur at $\omega = \omega_{2i-1}'(i=1,2\cdots)$, and $\omega = \omega_{2i}'/2(i=1,2,\cdots)$, respectively, for antisymmetric or horizontal motions in an identical direction. However, for the current fully nonlinear analysis, it is seen that no peak graphically appears at $\omega = \omega_{2i}'/2\,(i=1,2,\cdots)$.

Fig. 22 made further comparisons of maximum waves at $p_{r1}$ and forces in the $x$-direction at five Froude numbers $F_n$=-0.128, -0.64, 0, 0.064 and 0.128. It can be seen from Fig. 22a that the magnitudes of five main peaks of waves at the oscillational frequencies $\omega_1''$ do not change too much when the Froude number increases or decreases，However, the peaks at $\omega_3''$ and $\omega_5''$ clearly decrease as the absolute value of $F_n$ increases. As pointed out by Wang and Wu [12], Wang et al. [14], Huang and Wang [33]， no resonance happen at $\omega = \omega_{2i}'(i = 1,2,\cdots)$ for horizontal motions in an identical direction when $F_n$=0. However, it is interesting to see that four bigger peaks at $\omega_2''$ and four smaller peaks at $\omega_4''$ appear when $F_n \neq 0$ and $\omega_2''/\omega_2$ & $\omega_4''/\omega_2$ are approximately 1.396, 1.415, 1.415 & 1.398, as well as 1.94, 1.98, 1.98 & 1.93 for $F_n$=-0.128, -0.064, 0.064 & 0.128, respectively. It can be seen that the peak at $\omega_2''$ also increases as the increase of the absolute value of $F_n$ and that at $\omega_4''$ increases as the increase of $F_n$. Similarity can be also for the forces in Fig. 22b.

Fig. 23 gives the waves versus $\omega/\omega_1$ at $A/d$=0.0125 and 0.05 to exhibit the nonlinearities of waves and forces at different resonant frequencies. Just like the situations of vertical oscillations, the maximum nondimensionalized waves decreases as the increase of $F_n$ at $\omega_i''/\omega_1 (i = 1,2,\cdots,5)$ and each $\omega_i''/\omega_1$ at $A/d$=0.05 are generally smaller than those at $A/d$=0.0125. The corresponding hydrodynamic forces on cylinder 1 are given in Fig. 24 and similarity can be found.

Similar to the analyses about Keulegan-Carpenter number in Fig. 19, the maximum wave peak $\eta_{\max}$ is about 37.7$A$ at $\omega_1''$, $A/d$=0.05 and $Fn$=-0.128 in Fig. 23, and its corresponding Keulegan-Carpenter number is 2.96, which is also less than 3. Hence, the simulations of the horizontal motions are also valid.

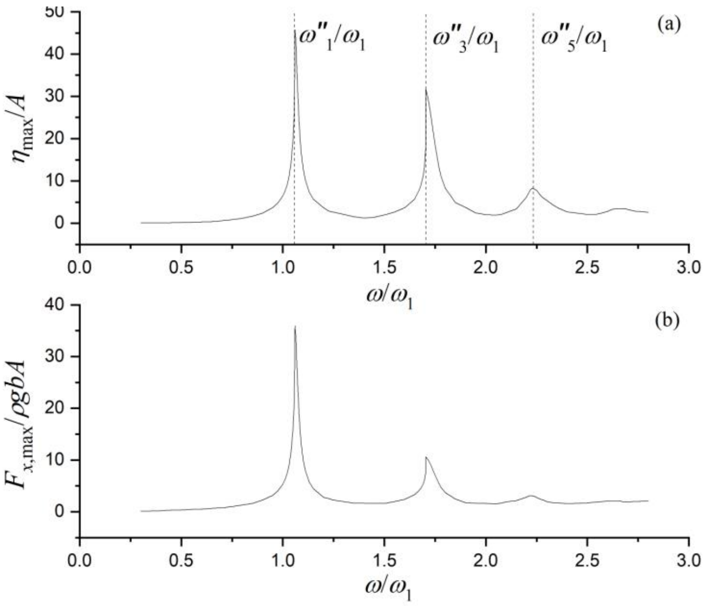


**Fig. 21.** Maximum values of waves at $p_{r1}$ and maximum horizontal forces on cylinder 1 versus $\omega / \omega_1$ at $F_n$=0.

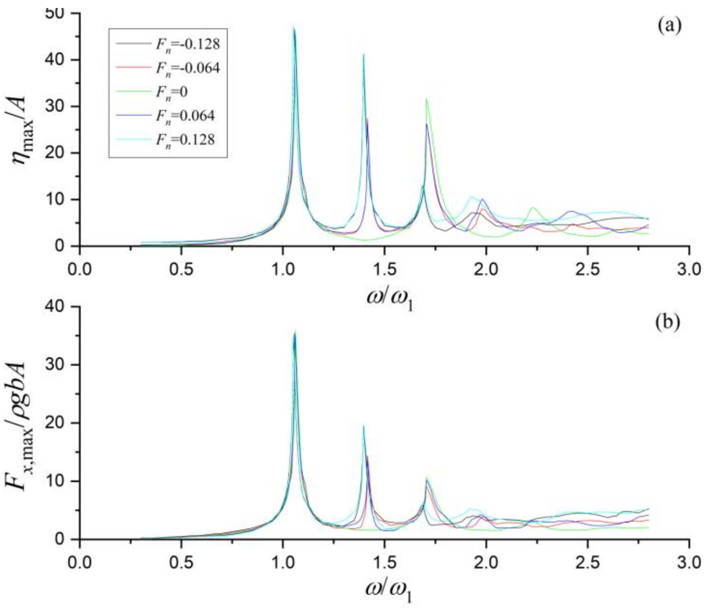


**Fig. 22.** Maximum values of waves at $p_{r1}$ and maximum horizontal forces on cylinder 1 versus $\omega / \omega_1$.

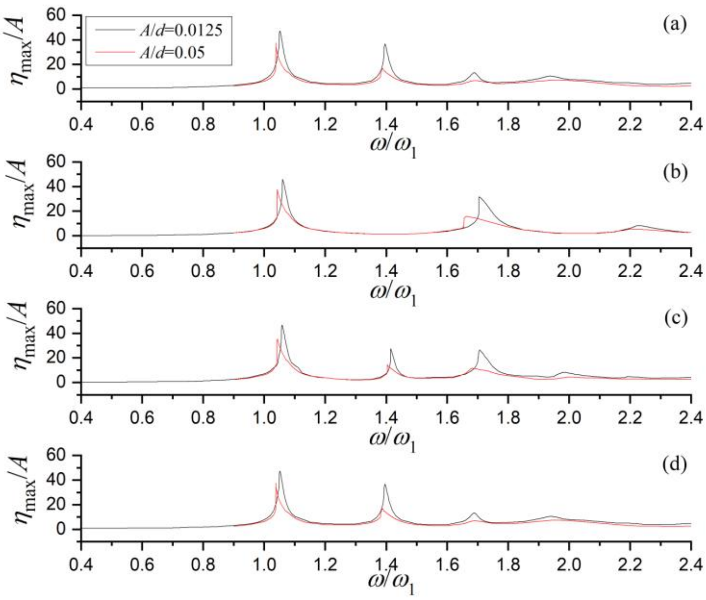


**Fig. 23.** Comparisons of maximum values of waves at $p_{r1}$ versus $\omega/\omega_1$ at $A/d$=0.0125 & 0.05; (a) $F_n$=-0.128; (b) $F_n$=0; (c) $F_n$=0.064; (d) $F_n$=0.128.

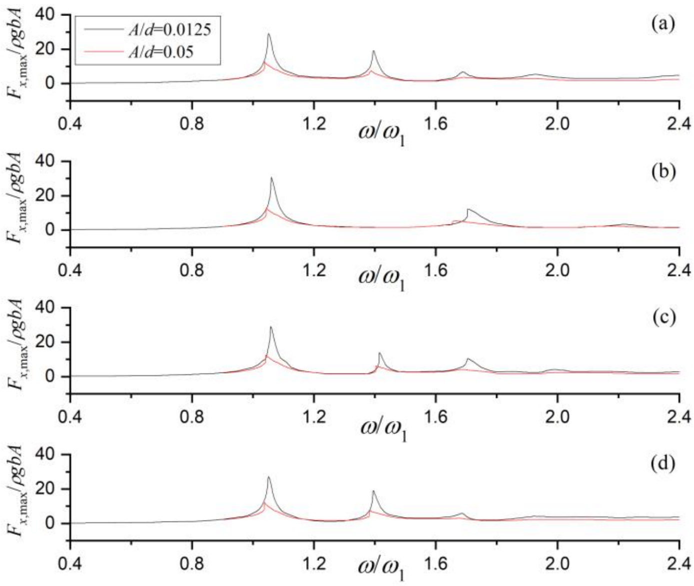


**Fig. 24.** Maximum horizontal forces on (a) cylinder 1 versus $\omega/\omega_1$ at $A/d$=0.0125 & 0.05; (a) $F_n$=-0.128; (b) $F_n$=0; (c) $F_n$=0.064; (d) $F_n$=0.128.

Simulations at $l_c/b$ =5, 6, 7 and 9 are also made in addition to $l_c/b$ =8 for horizontal motions. The oscillational frequencies $\omega_1''/\omega_1$, $\omega_2''/\omega_1$ and $\omega_3''/\omega_1$ versus $l_c/b$ are given in Fig. 25. Four Froude numbers $F_n$=-0.128, 0, 0.064 and 0.128 are used. It can be seen that the nondimensionalized frequency at each Froude number is nearly linearly increases as $l_{cy}/b$

increases for $\omega_1''/\omega_1$ within the whole range of $l_c/b$ and for $\omega_2''/\omega_1$ when $l_{cy}/b$>6, and it becomes smaller as the absolute value of $F_n$ increases at each $l_{cy}/b$ (see Figs. 25a, 25b).

The maximum waves and horizontal forces on cylinder 1 as functions of $l_c/b$ at $\omega_1''$, $\omega_3''$ and $\omega_2''$ are shown in Figs. 26 and 27. The maximum waves at $\omega_1''$ in Fig. 26a decrease as the increase of $l_c/b$ at each Froude numbers and they are clearly different at smaller $l_c/b$ and then they almost coincide with each other when $l_c/b\geqslant 7$. The horizontal forces given in Fig. 26b, however, show more complicate change with the spacing and the Froude number. All maximum values are at $l_c/b$=7 and they decline at other values of $l_c/b$. The maximum waves and forces at $\omega_3''$ generally increase as the increase of $l_c/b$ and decrease as the absolute value of $F_n$ at each $l_c/b$. As to the situation at $\omega_2''$, the cases at $F_n$=-0.128, 0.064 and 0.128 are given in Fig. 27, in which the results at $F_n$=0 are not provided because of no resonance happens and hence there is no peak. It can be seen that both maximum wave and force gradually grow up as the spacing $l_c/b$ becomes larger at every $F_n$, and they are generally enlarged with the increase of the absolute value of $F_n$ at every $l_c/b$.

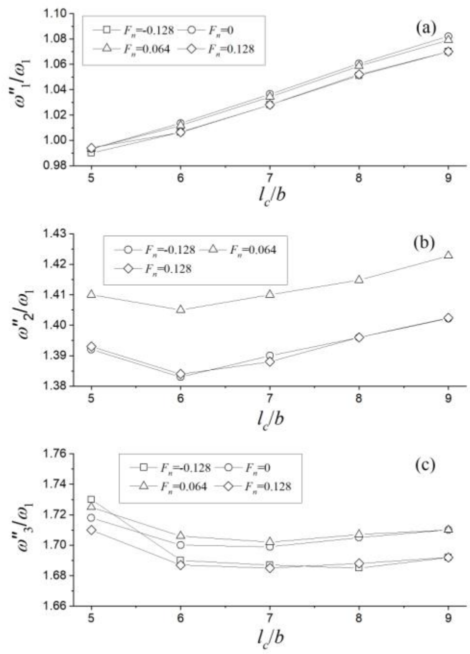


**Fig. 25.** The oscillational frequency at resonance versus $l_c/b$ in horizontal motions; (a) $\omega_1''/\omega_1$; (b) $\omega_2''/\omega_1$; (c) $\omega_3''/\omega_1$.

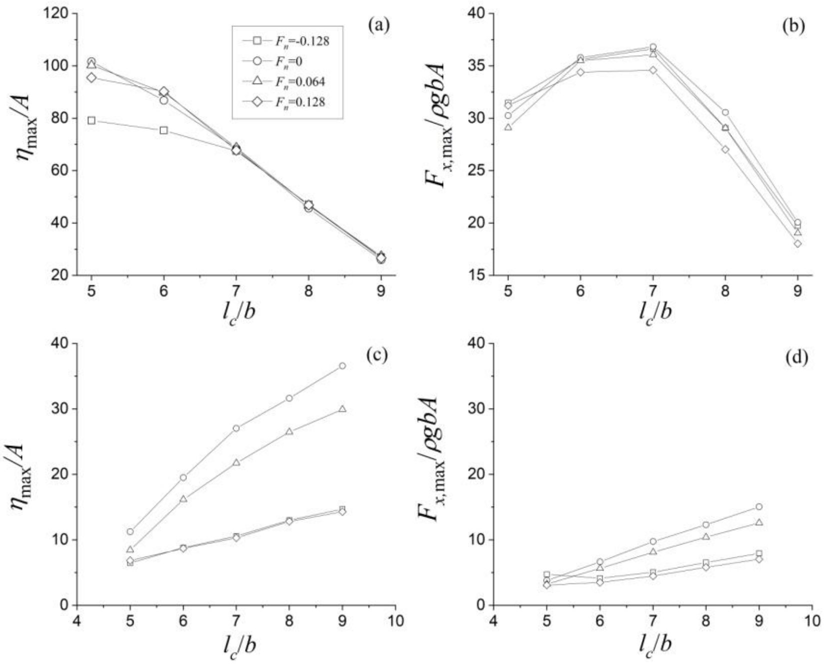


**Fig. 26.** Maximum waves and horizontal forces versus $L_{cy}/b$ at $\omega_1'$ and $\omega_3'$; (a) waves at $p_{r1}$ at $\omega_1''$; (b) horizontal forces on cylinder 1 at $\omega_1''$; (c) waves at $p_{r1}$ at $\omega_3''$; (d) horizontal forces on cylinder 1 at $\omega_3''$.

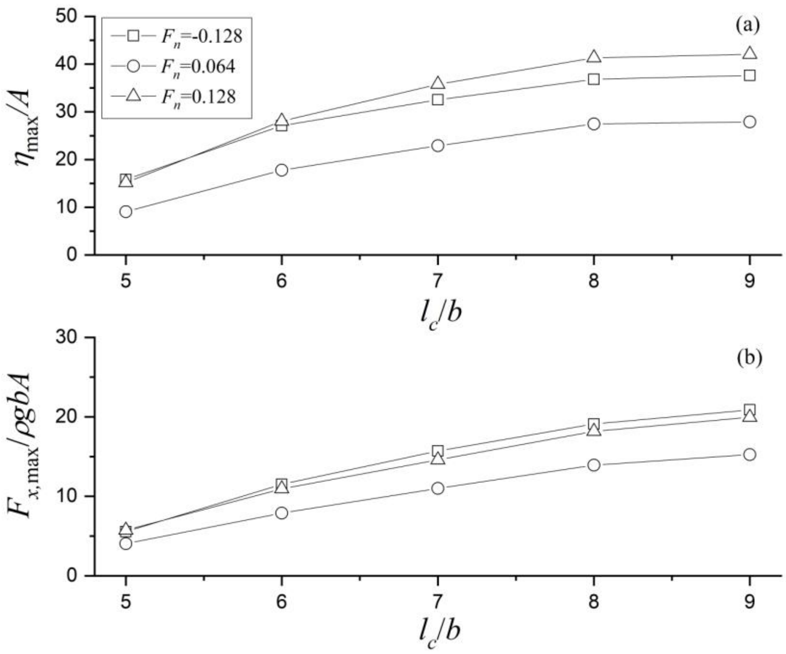


**Fig. 27.** Maximum waves and horizontal forces versus $L_{cy}/b$ at $\omega_2''$ in horizontal motions; (a) waves at the right side of cylinder 1; (b) horizontal forces on cylinder 1.

## 5. Conclusions

A fully nonlinear potential flow model based on a higher order finite element method with 8-node curve element is used to analyse the wave resonance between twin cylinders in specified oscillations in a uniform current. The 4th order Runge-Kutta algorithm is employed to track the node positions and corresponding potentials on them at each time step. A damping zone method is used for satisfying the radiation condition.

Numerical simulations have been made for twin rectangular cylinders in the free surface in vertical and horizontal motions in a uniform current at resonant frequencies. Waves and hydrodynamic forces are calculated, and comparisons are made at different Froude numbers. The current effect on the wave and force has been analysed at odd and even-order resonances. Besides, the nonlinearity of the wave and forces are also discussed. The simulation shows the current has a critical influence on the waves and forces at resonant frequencies in both vertical and horizontal oscillations. The conclusion of this study is summarized as below:

As discussed in Section 4, the first and second order resonances happen at $\omega'_{2i}\ (i=1,2,...)$ and $\omega'_{2i}/2\ (i=1,2,...)$, respectively, for vertical oscillations or the horizontal in opposite directions at $F_n$=0. Similarly, the first and second order resonances also occur at $\omega=\omega'_{2i-1}\ (i=1,2\cdots)$, and $\omega=\omega'_{2i}/2\ (i=1,2,\cdots)$, respectively, for horizontal oscillations in an identical direction at $F_n$=0. However, when a current exists or $F_n \neq 0$, it is found that the first order resonance happens at all frequencies $\omega''_i(i=1,2,...)$ for both vertical and horizontal motion, and the second-order resonant effect is generally weak. For the vertical motions, the maximum wave and horizontal force at $\omega''_{2i}\ (i=1,2)$ become smaller as $F_n$ increases. However，they are clearly increases as the increase of $F_n$ at $\omega''_{2i\text{-}1}\ (i=1,2)$; For the horizontal motions, the maximum wave and horizontal force have only a little change as $F_n$ changes at $\omega''_1$, which is not regular. However, they generally decrease at $\omega''_3$ and increase at $\omega''_2$ as the increase of the absolute value of $F_n$.

The oscillational frequencies $\omega''_i(i=1,2,3)$ and $\omega''_{2\mathrm{h}}$ at resonance become somewhat smaller as the increase of $F_n$ in vertical motions and $\omega''_i(i=1,2)$ decrease as the increase of the absolute value of $F_n$ in horizontal motions within the whole range of $l_c/b$. Besides, they generally increase as $l_c/b$ when $l_c/b \geq 6$ for both vertical and horizontal motions.

The wave and force at $\omega_i''(i=1,2...)$ versus the spacing $l_c/b$ are also studied. For vertical motions, the maximum values of wave and horizontal force at $\omega_2''$ always enhance as the increases of $l_c/b$ at every $F_n$, and they are generally decline or increase as the increases of $l_c/b$ within $l_c/b \geq 6$ at $\omega_1''$ or $\omega_3''$, respectively; For horizontal motions, as $l_c/b$ increases, the maximum value of wave at $\omega_1''$ decreases as the increases of $l_c/b$ at every $F_n$. By contrast, both the maximum wave and force increase as the increases of $l_c/b$ at $\omega_i''(i=2,3)$.

For oscillations of both cylinders in larger amplitudes, the oscillational frequencies $\omega_i''(i=1,2,...)$ are clearly smaller than those under smaller amplitude oscillations, and the nondimensionalized maximum values of wave and horizontal force become smaller under larger amplitude oscillations, which weakens resonant characteristics.

## Acknowledgement

The authors wish to express our appreciation for the support from the National Natural Science Foundation of China (Grant No. 52171325, 51679096). The second author is also sponsored by the joint scholarship form Lloyd's Register Foundation and China Scholarships Council, to which he is most grateful.

## Data availability statement

The data that supports the findings of this study is available within the article.

## References

[1] G.X. Wu. Second-order resonance of sloshing in a tank. Ocean engineering. 2007;34:2345-9.

[2] H.S. Zhang, P.F. Wu, W.B. Liu. The analysis of second-order sloshing resonance in a 3-D tank. Journal of Hydrodynamics. 2014;26:309-15.

[3] H.D. Maniar, J.N. Newman. Wave diffraction by a long array of cylinders. Journal of fluid mechanics. 1997;339:309-30.

[4] D.V. Evans, R. Porter. Near-trapping of waves by circular arrays of vertical cylinders.

Applied Ocean Research. 1997;19:83-99.

[5] J.T. Chen, J.W. Lee. A semi-analytical method for near-trapped mode and fictitious frequencies of multiple scattering by an array of elliptical cylinders in water waves. Physics of Fluids. 2013;25:097103.

[6] Š. Malenica, R. Eatock Taylor, J.B. Huang. Second-order water wave diffraction by an array of vertical cylinders. Journal of Fluid Mechanics. 1999;390.

[7] C.Z. Wang, G.X. Wu. Time domain analysis of second-order wave diffraction by an array of vertical cylinders. Journal of Fluids and Structures. 2007;23:605-31.

[8] H. Kagemoto, M. Murai, T. Fujii. Second-order resonance among an array of two rows of vertical circular cylinders. Applied Ocean Research. 2014;47:192-8.

[9] L. Sun, R. Eatock Taylor, P.H. Taylor. First-and second-order analysis of resonant waves between adjacent barges. Journal of Fluids and Structures. 2010;26:954-78.

[10] R.A. Watai, P. Dinoi, F. Ruggeri, A. Souto-Iglesias, A.N. Simos. Rankine time-domain method with application to side-by-side gap flow modeling. Applied Ocean Research. 2015;50:69-90.

[11] W. Zhao, Z. Pan, F. Lin, B. Li, P.H. Taylor, M. Efthymiou. Estimation of gap resonance relevant to side-by-side offloading. Ocean Engineering. 2018;153:1-9.

[12] C.Z. Wang, G.X. Wu. Analysis of second-order resonance in wave interactions with floating bodies through a finite-element method. Ocean Engineering. 2008;35:717-26.

[13] C.Z. Wang, G.X. Wu, B.C. Khoo. Fully nonlinear simulation of resonant motion of liquid confined between floating structures. Computers & fluids. 2011;44:89-101.

[14] C.Z. Wang, Q.C. Meng, H.C. Huang, B.C. Khoo. Finite element analysis of nonlinear wave resonance by multiple cylinders in vertical motions. Computers & Fluids. 2013;88:557-68.

[15] Y.J. Li, C.W. Zhang. Analysis of wave resonance in gap between two heaving barges. Ocean engineering. 2016;117:210-20.

[16] D. Sen. Time domain simulation of side-by-side floating bodies using a 3D numerical wave tank approach. Applied Ocean Research. 2016;58:189-217.

[17] W. Bai, X. Feng, R. Eatock Taylor, K.K. Ang. Fully nonlinear analysis of near-trapping phenomenon around an array of cylinders. Applied Ocean Research. 2014;44:71-81.

[18] D.Z. Ning, X.J. Su, M. Zhao, B. Teng. Numerical study of resonance induced by wave action on multiple rectangular boxes with narrow gaps. Acta Oceanologica Sinica. 2015;34:92-102.

[19] X. Feng, W. Bai. Wave resonances in a narrow gap between two barges using fully nonlinear numerical simulation. Applied Ocean Research. 2015;50:119-29.

[20] H.C. Wang, W.H. Zhao, S. Draper, H.A. Wolgamot, P.H. Taylor. Experimental and numerical study of free-surface wave resonance in the gap between two elongated parallel boxes with square corners. Applied Ocean Research. 2020;104:102376.

[21] W.H. Zhao, P.H. Taylor, H.A. Wolgamot, B. Molin, R. Eatock Taylor. Group dynamics and wave resonances in a narrow gap: modes and reduced group velocity. Journal of Fluid Mechanics. 2020;883.

[22] L. Lu, X.B. Chen. Dissipation in the gap resonance between two bodies. Proceedings of the 27th International Workshop on Water Waves and Floating Bodies (IWWWFB 2012): Citeseer; 2012.

[23] L. Lu, B. Teng, L. Sun, B. Chen. Modelling of multi-bodies in close proximity under water waves—Fluid forces on floating bodies. Ocean Engineering. 2011;38:1403-16.
[24] K.H. Chua, R. Eatock Taylor, Y.S. Choo. Hydrodynamic interaction of side-by-side floating bodies part I: Development of CFD-based numerical analysis framework and modified potential flow model. Ocean Engineering. 2018;166:404-15.
[25] S.C. Jiang, W. Bai, G.Q. Tang. Numerical simulation of wave resonance in the narrow gap between two non-identical boxes. Ocean Engineering. 2018;156:38-60.
[26] B. Büchmann, P. Ferrant, J. Skourup. Run-up on a body in waves and current. Fully nonlinear and finite-order calculations. Applied ocean research. 2000;22:349-60.
[27] M.S. Celebi. Nonlinear transient wave–body interactions in steady uniform currents. Computer methods in applied mechanics and engineering. 2001;190:5149-72.
[28] S. Ryu, M.H. Kim, P.J. Lynett. Fully nonlinear wave-current interactions and kinematics by a BEM-based numerical wave tank. Computational mechanics. 2003;32:336-46.
[29] W. Koo, M.-H. Kim. Current effects on nonlinear wave-body interactions by a 2D fully nonlinear numerical wave tank. Journal of waterway, port, coastal, and ocean engineering. 2007;133:136-46.
[30] L. Zhen, B. Teng, D.Z. Ning, G. Ying. Wave-current interactions with three-dimensional floating bodies. Journal of Hydrodynamics, Ser B. 2010;22:229-40.
[31] Y.L. Shao, O.M. Faltinsen. Second-order diffraction and radiation of a floating body with small forward speed. Journal of offshore mechanics and Arctic engineering. 2013;135.
[32] A.G. Fredriksen, T. Kristiansen, O.M. Faltinsen. Experimental and numerical investigation of wave resonance in moonpools at low forward speed. Applied Ocean Research. 2014;47:28-46.
[33] H.C. Huang, C.Z. Wang. Finite element simulations of second order wave resonance by motions of two bodies in a steady current. Ocean Engineering. 2020;196:106734.
[34] Y.F. Yang, C.Z. Wang. Finite element analysis of second order wave resonance by multiple cylinders in a uniform current. Applied Ocean Research. 2020;100:102132.
[35] G.X. Wu. Hydrodynamic force on a rigid body during impact with liquid. Journal of Fluids and Structures. 1998;12:549-59.
[36] G.X. Wu, R. Eatock Taylor. The coupled finite element and boundary element analysis of nonlinear interactions between waves and bodies. Ocean Engineering. 2003;30:387-400.
[37] C.Z. Wang, G.X. Wu. An unstructured-mesh-based finite element simulation of wave interactions with non-wall-sided bodies. Journal of fluids and structures. 2006;22:441-61.
[38] M. Isaacson, K.F. Cheung. Time-domain solution for wave—current interactions with a two-dimensional body. Applied Ocean Research. 1993;15:39-52.